A Transmitter-Embedded Metasurface-Based Wireless Power Transfer System for Extended-Distance Applications

Yuanxi Chen, *Student Member, IEEE*, Xing Zhao, *Member, IEEE*, Shuangxia Niu, *Senior Member, IEEE*, Weinong Fu, and Hongjian Lin, *Senior Member, IEEE*

***Abstract*—Portability and efficiency are crucial parameters in wireless power transfer (WPT) systems for extended-distance wireless applications. However, these systems often face challenges of low efficiency and mutual inductance. Generalized solutions employ ferrite, intermediate coils, metamaterials, or increasing operating frequency to address these issues. However, those solutions always lead to poor portability with extra weight and volume, except for increasing the operating frequency. To tackle these challenges, this article proposes a transmitter-embedded metasurface (TEMS) for the WPT system. The design aims to increase efficiency and the coupling coefficient under high operating frequency while maintaining a lightweight and occupying no extra volume, based on the negative permeability property. The *L*/*C*-based mathematical model and parametric investigations are conducted to explore the negative permeability property of TEMS. A prototype of the TEMS-based WPT system is implemented to validate the effect of TEMS on efficiency and coupling coefficient enhancement. The experimental results demonstrate that the proposed design can increase efficiency by at least 14.5% over transfer distances longer than 125 mm.**

***Index Terms*—Extended-distance, negative permeability, transmitter-embedded metasurface (TEMS), wireless power transfer (WPT).**

I. Introduction

WIRELESS power transfer (WPT) technology [1], [2], [3], [4] is a research focus for a decade for its flexibility, safety, reliability, and better convenience [5], having broad prospects in relevant electric applications [6], [7]. For those extended transmission distance WPT systems, excepting the operating frequency improvement, ferrite [8], intermediate coil [9], and metamaterial/metasurface [10], [11], [12], [13], [14] are the most well-explored solutions to enhance the efficiency of the systems. The megahertz (MHz) WPT systems inherent have the efficiency advantage under extended transfer distance, for the efficiency is proportional to the mutual inductance between coils and the operating frequency of the system [15]. Similarly, the loss of the ferrite also boosts with the increase of the frequency, limiting its application in the MHz WPT system. The copper-based intermediate coil/resonator and metamaterial/metasurface can enhance the efficiency under the high-frequency region, becoming a research hotpot in this decade.

Regarding wireless power transfer systems with intermediate coils or resonators [16], [17], [18], [19], Liu and Wang [16] explored the use of double intermediate resonant coils, achieving an efficiency of 72.4% in a 4.63 MHz WPT system under an extended transfer distance. Li et al. [17] proposed a 13.56 MHz WPT system with multiple coupling paths, enhancing efficiency even over transfer distances greater than the diameter of the coils. A superconductivity intermediate coil is proposed in Oshimoto et al. [18], which increases the efficiency from 17.5% to 49.7%.

As for the metamaterial/metasurface, based on the properties being utilized, the 2-D metasurface and 3-D metamaterial [20] used in MHz WPT systems can be broadly classified into two types: transmission-type and reflection-type. The transmission type employs the transmission property of the metamaterial with negative or near zero permeability while the reflection type employs its reflection properties with zero permeability solely. These properties can be designed by modifying the operating frequency of the WPT system and/or the resonant frequency of the metamaterial/metasurface. Regarding the transmission type [21], [22], [23], [24], the metamaterial slab is typically placed between the transmitter and receiver coils in a parallel orientation. Yang et al. [21] and Cho et al. [22] explored the feasibility of utilizing hybrid metamaterial units with zero or negative permeability to enhance efficiency, resulting in a further 10.4% improvement compared to solutions that only incorporate negative permeability. The utilization of dual metamaterial slabs is discussed in Shaw and Mitra [23], indicating a 16.4% increase in efficiency. Moreover, Lu et al. [24] proposed a dual-band double-layer metamaterial with negative and near-zero

Manuscript received 25 March 2023; revised 23 July 2023 and 30 August 2023; accepted 24 September 2023. Date of publication 29 September 2023; date of current version 6 December 2023. This work was supported by the Research Grant Council of the Hong Kong SAR Government under Grant PolyU152180/19E. Recommended for publication by Associate Editor F. Lu. *(Corresponding author: Shuangxia Niu.)*

Yuanxi Chen and Shuangxia Niu are with the Department of Electrical Engineering, The Hong Kong Polytechnic University, Hong Kong (e-mail: 19109864r@connect.polyu.hk; eesxniu@polyu.edu.hk).

Xing Zhao is with the Department of Electronic Engineering, University of York, YO10 5DD York, U.K. (e-mail: xing.zhao@york.ac.uk).

Weinong Fu is with the Shenzhen Institutes of Advanced Technology, Chinese Academy of Sciences, Shenzhen 518038, China (e-mail: wn.fu@siat.ac.cn).

Hongjian Lin is with the City University of Hong Kong, Hong Kong (e-mail: hongjian_lin@ieee.org).

Color versions of one or more figures in this article are available at https://doi.org/10.1109/TPEL.2023.3320743.

Digital Object Identifier 10.1109/TPEL.2023.3320743

TABLE I
COMPREHENSIVE BETWEEN THE PROPOSED TEMS AND STATE-OF-ART WORKS FOR EXTENDED-DISTANCE WPT SYSTEMS

Categorization	No Additional Space Occupying	Applicable to High-frequency (MHz)	No unconventional material required	Lightweight	Strong Universality
This paper: TEMS	√	√	√	√	√
[8]: Ferrite	√(nearly)	×	√	×	√
[16]: Double intermediate coils	×	√	√	×	√
[17]: Single resonator	√(nearly)	√	√	√	×
[18]: Superconductivity resonator	×	√	×	√	×
[21]: Single MTM in the middle	×	√	√	√	×
[24]: Dual-band middle MTM	×	√	√	√	×
[26]: Dual MTM in back side	×	√	√	×	√
[29]: Cubic MTM in the middle	×	√	√	√	×

permeability, showcasing a 10%–15% increase in efficiency at two distinct operating frequencies, 13.56 MHz and 27.12 MHz.

In the case of WPT systems with reflection-type metamaterial/metasurface [25], [26], the slab can be positioned either outside or vertically to the transmitter and receiver. Lu et al. [25] proposed dual side-placed metasurface slabs, to suppress the electromagnetic fields leakage in the MHz WPT system and increase the efficiency by 27.2%. The metasurface slab in Lu et al. [26] is installed on both outer sides of the WPT system and achieved a 12.06% efficiency increase. Compared to the topologies of transmission type, the topologies in [25] and [26] have better practicability for they do not occupy the space in the transmission path. While generalized solutions have been effective in promoting efficiency, their installation always requires space outside the transmitter and receiver, decreasing the flexibility and portability of WPT systems.

To address the abovementioned issues, in this article, a transmitter-embedded metasurface (TEMS) is proposed. To better indicate the superiority of the proposed TEMS, a comprehensive comparison with state-of-art works is given in Table I. As indicated in Table I, the proposed TEMS have comprehensive advantages compared to previously proposed solutions, i.e., the proposed TEMS has the strength in lightweight and high-frequency applicability compared to ferrite material [8]. In contrast to the metamaterial/metasurface-based [21], [24], [26], [29] and resonator-based [16], [17] solutions, the proposed TEMS occupies no additional space to install the slabs. Moreover, the proposed TEMS manufactured by the FR4 slab, copper wire, and compensation capacitor, which does not rely on unconventional materials compared to the solution in [18]. Based on the abovementioned issues, the salient merits of the TEMS are concluded as follows.

1) The portability and flexibility are enhanced compared to WPT systems with resonators and generalized metamaterial /metasurface. The proposed TEMS occupy no additional space excluding the occupation of the transmitter coil.
2) The high-efficiency enhancement capability is achieved with a reduced volume, for all the magnetic fields generated by the transmitter must cross through the TEMS and accordingly, are modified.
3) A high level of integration is achieved with the proposed design. The proposed design encapsulates TEMS together with the transmitter coil, while the generalized metasurface and intermedia coil are not. This design avoids the issue of compensation network selection being affected by the varying distance between the metasurface and the transmitter coil.

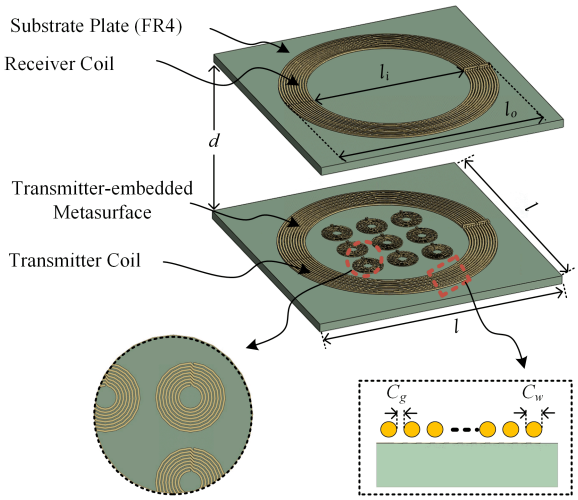

Fig. 1. Schematic diagram of TEMS based WPT system.

II. ANALYSIS AND DESIGN OF THE TRANSMITTER-EMBEDDED METASURFACE

A. Structure Design and Overall Analysis

The schematic diagram and geometric definition of the TEMS-based WPT system is shown in Fig. 1, which consists of a receiver, transmitter, and the TEMS slab separated at a transfer distance d. The installation position of the TEMS ensures that all the magnetic fields generated by the transmitter will be modified by the TEMS. The detailed geometric parameters of the transmitter, receiver, TEMS, and TEMS unit, are given in Fig. 2 and Table II. The geometric parameters and number of turns of the receiver are as same as a transmitter.

The material of the transmitter/receiver coil and TEMS unit is copper while that of the substrate plate is FR4, which has the same permeability as air. The length l of the substrate plate and that of the proposed TEMS l_m is 150 and 94 mm, respectively.

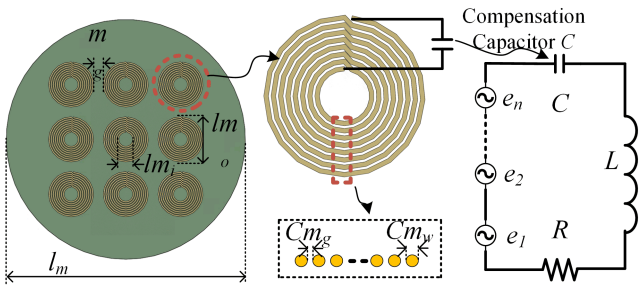

Fig. 2. Diagrammatic drawing of the proposed TEMS. (a) Proposed TEMS. (b) TEMS unit. (c) Equivalent circuit of the TEMS units.

TABLE II
GEOMETRIC PARAMETERS OF TRANSMITTER/RECEIVER AND TEMS

Defination	Symbol	Transmitter/ Receiver	Symbol	TEMS unit
Inner diameter (mm)	l_i	94	l_m	6
External diameter (mm)	l_o	124	l_{mo}	15.8
Coil turns width (mm)	c_w	1	c_{mw}	0.6
Coil turns gap (mm)	c_g	1.5	c_{mg}	0.8
Number of turns	N	11	N	8
Resistance (Ω)	R_i	1.94	R_m	0.33
Self-inductance (uH)	L_i	21.3	L_m	1.37
Compensation capacitor (pF)	C_i	6.5	C_m	125

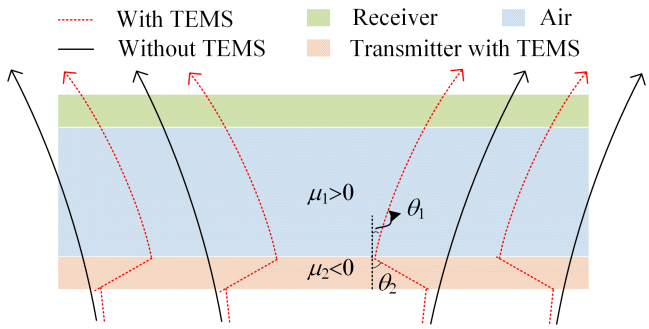

Fig. 3. Diagrammatic drawing of the proposed TEMS.

The designed metasurface slab, unit and its equivalent circuit are shown in Fig. 2. The equivalent circuit metasurface unit consists of the resistor, compensation capacitor, inductance, and the induced voltages generated by the transmitter, receiver, and another metasurface unit (e_1, e_2·····e_n).

The diagrammatic drawing of the TEMS in the WPT system is indicated in Fig. 3. As shown in Fig. 3, the magnetic field will be modified by the TEMS and the corresponding leakage flux will be reduced, for more magnetic field lines go through the receiver, accordingly, the magnetic induction intensity of the receiver will be increased.

B. Analysis of Double-Negative Metasurface

The metamaterials/metasurface are divided into four regions in terms of the polarities of permittivity and permeability [27], [32], including conventional double-positive material, epsilon-negative material, mu-negative material, and double-negative (DNG) material.

All metasurface, including the proposed structure, should follow the basic rule [21] given as follows:

$$\frac{\tan\theta_1}{\tan\theta_2} = \frac{\mu_1}{\mu_2} \tag{1}$$

where θ_1 and θ_2 are the refractive angles at two sides of materials, while μ_1, μ_2 are the corresponding permeability of two materials, which can be found in Fig. 3.

The black dashed lines and the black solid lines in the quadrant of Fig. 3 represent the magnetic field crossing through the metasurface with negative permeability and permittivity. It is used to guide the propagation of waves and fields, as well as focus the near field, correspondingly improving the magnetic field strength around the receiver. The overall analysis of the metasurface considering the magnetic circuit interaction is given as follows.

As shown in Fig. 2(a), Kirchhoff's voltage equation of the metasurface unit is obtained as

$$I\left(R + \frac{1}{j\omega C} + j\omega L\right) = e + \sum_{p=1}^{n} e_p \tag{2}$$

where R, C, and L, are the resistor, compensation capacitor, and equivalent inductance of the metasurface, respectively. e and $\sum_{p=1}^{n} e_p$ are the voltages induced by the transmitter, receive and other metasurface units.

The voltage in (2) is induced by the variation of the flux, following:

$$e + \sum_{p=1}^{n} e_p dp = -\frac{d}{dt}\sum_{k=1}^{m}\int_{s,k}\left[\left(B_{e,k} + \sum_{l=1}^{n} B_{n,k}\right) ds_k\right] \tag{3}$$

where $B_{e,k}$ and $B_{n,k}$ is the magnetic strength induced by the kth turns of the transmitter coil and metasurface units. s_k is the area of the metasurface unit. m and n are the numbers of turns of the transmitter and metasurface units.

The relationship between magnetic strength $B_{e,k}$, $B_{n,k}$ and corresponding magnetic field intensity $H_{e,k}$ and $H_{e,k}$ is as follows:

$$B_{e,k} = u_0\, u_r\, H_{e,k} = \mu H_{e,k} \tag{4}$$

$$B_{n,k} = u_0\, u_r\, H_{n,k} = \mu H_{n,k} \tag{5}$$

where u_0 and u_r are the vacuum and the relevant permeability of the material.

Tanking (3) into (2), the current flowing through the metasurface can be expressed

$$I = \frac{1}{L}\frac{\omega^2}{\omega_0^2 - \omega^2 + j\frac{R\omega}{L}}\sum_{k=1}^{m}\int_{s,k}\left[\left(B_{e,k} + \sum_{l=1}^{n} B_{n,k}\right) ds_k\right] \tag{6}$$

where ω_0 is the resonant frequency of the metasurface unit, which should satisfy the following equation:

$$\omega_0 = \frac{1}{\sqrt{LC}}. \tag{7}$$

The magnetization intensity M is defined by

$$M = \frac{I\sum_{k=1}^{m} S_k}{V} e_m \tag{8}$$

where V is the volume of the metasurface unit and S_k is the area surrounded by each coil turn of the metasurface. e_m is the magnetic dipole moment.

Taking (6) into (8), the magnetization intensity M is redefined as

$$M = \frac{1}{LV}\frac{\omega^2}{\omega_0^2-\omega^2+j\frac{R\omega}{L}}\sum_{k=1}^{m}\int_{s,k}\left[\left(B_{e,k}+\sum_{l=1}^{n}B_{n,k}\right)ds_k\right]s_k. \tag{9}$$

The relative permeability of the metasurface can be obtained via the magnetization intensity, defined as follows:

$$\mu_r = \left(1+\frac{M}{H}\right) = 1+X_v \tag{10}$$

where X_v is the volume magnetic susceptibility and μ_r is the relative permeability of the metasurface unit.

By taking (9) and (8) with (10), the relative permeability related to the transmitter coil and other metasurface units is given as follows:

$$\mu_{re} = 1+\frac{\mu_0}{LV}\frac{\omega^2}{\omega_0^2-\omega^2+j\frac{R\omega}{L}}\sum_{k=1}^{m}\int_{s,k}\left[s_k+\sum_{l=1}^{n}\frac{H_{n,k}}{H_{e,k}}s_k\right]s_k$$
$$\mu_{rn} = 1+\frac{\mu_0}{LV}\frac{\omega^2}{\omega_0^2-\omega^2+j\frac{R\omega}{L}}\sum_{k=1}^{m}\int_{s,k}\left[\frac{H_{e,k}}{H_{n,k}}s_k+\sum_{l=1}^{n}s_k\right]s_k \tag{11}$$

where μ_{re} and μ_{rn} are the relative permeability of the metasurface related to the transmitter coil and other metasurface units.

The magnetic reluctance is calculated via the permeability μ, defined as

$$R_m = \frac{l}{\mu_0\mu_r A} \tag{12}$$

where R_m, l, and A are the magnetic reluctance, length, and cross area of the magnetic circuit, respectively.

Considering the magnetic circuit of the measured metasurface unit and transmitter coil, as well as that with the other metasurface units, is in parallel. The magnetic reluctance of the metasurface is redefined as

$$R_m = R_{me}//R_{mn} = \frac{l_e l_n}{A(l_n u_{re}+l_e u_{rn})} \tag{13}$$

where R_{me} and R_{mn} is the magnetic reluctance associated with the transmitter and other metasurface units.

In previously proposed solutions, the 2-D metasurface can be divided as planar [21], [22], [24], [26] and stacked structure [28]. As for the stacked metamaterial/metasurface, the relative permeability μ_r is obtained via (11), and (13) considering the units are tight intercoupling. Conversely, as for the planar metasurface, the coupling between units is loose compared to the stacked topology. Hence, the μ_{rn} are always ignored and the relative permeability of the metasurface is expressed as follows:

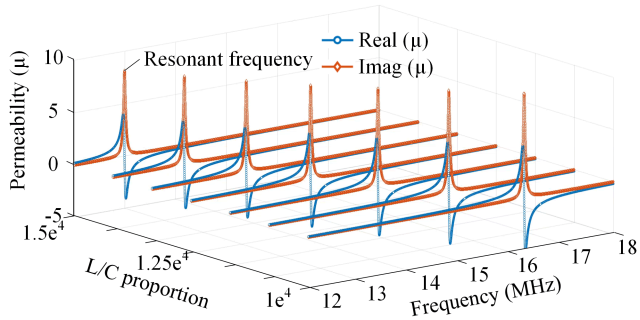

Fig. 4. Relationships between permeability, the proportion between equivalent inductance and compensation capacitor, as well as frequency.

$$\mu_r = 1+\frac{\mu_0}{LV}\frac{\omega^2}{\omega_0^2-\omega^2+j\frac{R\omega}{L}}\sum_{k=1}^{m}\int_{s,k}\left[s_k+\sum_{l=1}^{n}\frac{H_{n,k}}{H_{e,k}}s_k\right]s_k. \tag{14}$$

Based on (14), the impact of the *L/C* proportion of the metasurface on permeability is shown in Fig. 4. Under the resonant frequency, the real component of permeability is zero and the imaginary component of permeability reaches its peak value, respectively. When the operating frequency is higher than the resonant frequency, the real component of permeability will decrease sharply and move back to near zero after reaching the minimum value. The imaginary component of it will also decrease sharply and go down to zero directly. With the increase of the proportion of the equivalent inductance and compensation capacitor, the resonant frequency will increase and the corresponding permeability will also change. Hence, by regulating the *L/C* proportion of the metasurface, the desired permeability can be obtained. The real component corresponds to the property of the metasurface/metamaterial and the imaginary component is related to the loss. Under the resonance frequency, the imaginary component reaches its peak and the impedance reaches its minimum value, accordingly, the current peak at this condition with the largest loss.

Considering the self-inductance of the metasurface unit, the compensation capacitor is in the picofarad (pF) range, to ensure that the resonance frequency is lower than 13.56 MHz. Based on considerations of capacitor specifications, the compensation capacitor is selected as 100 pF.

The impact of the coil turns the number of the metasurface unit with the compensation capacitor of 100 pf on permeability is shown in Fig. 5(a) and (b).

In this article, the operating frequency is selected as 13.56 MHz, and the calculated results of operating frequency versus permeability are given in Fig. 6. Under the megahertz situation, the magnetic field is regarded as a quasi-static field, which means the electric field and magnetic field can be analyzed independently [21] and will not interact with each other. Based on Fig. 6(a) and (b), under the operation range near 13.56 MHz, the permittivity is always lower than zero and the DNG material (metasurface) is obtained, which can effectively refract the electromagnetic wave [27].

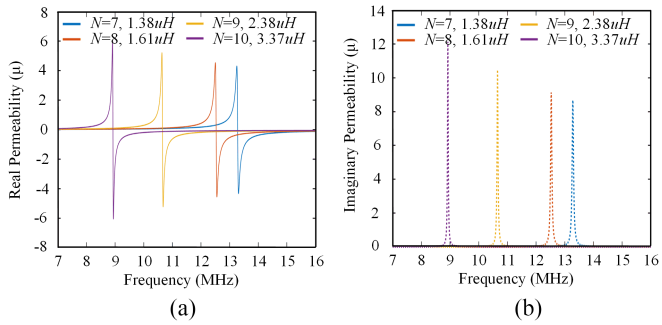

Fig. 5. Impact of number of turns of the metasurface on permeability. (a) Real component. (b) Imaginary component.

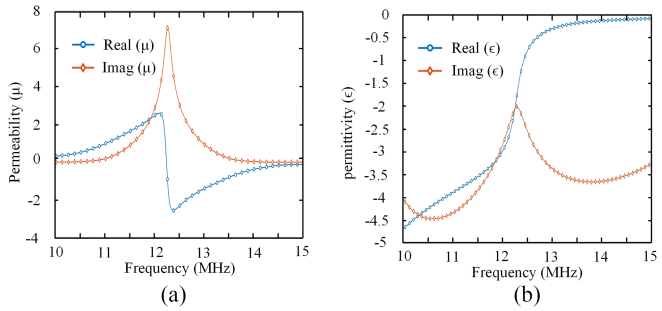

Fig. 6. Permeability and permittivity versus operating frequency of the designed metamaterial. (a) Permeability. (b) Permittivity.

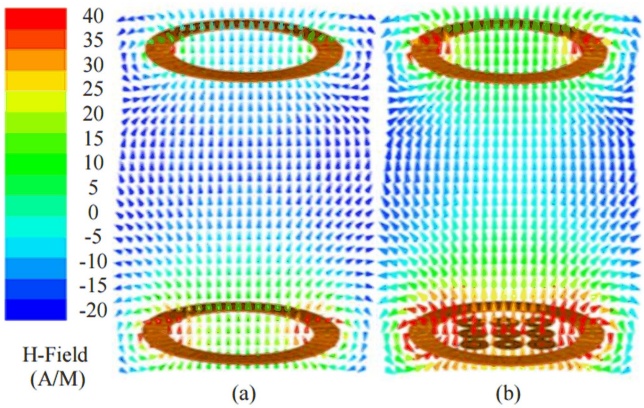

Fig. 7. Magnetic vector plot on transmission path of the WPT systems. (a) Without metamaterial. (b) With the proposed TEMS.

III. Simulation Analysis of the TEMS

In this part, the simulation analysis is conducted by the *Ansys*/HFSS. The simulations are conducted under the constant power condition and the load of the WPT systems with and without the proposed TEMS are the same. The magnetic vector plot with and without the TEMS is shown in Fig. 7(a) and (b). With the proposed TEMS, the magnetic field along the main magnetic circuit is enhanced.

The magnetic field strength distribution of the WPT system with and without the TEMS around the transmitter is given in Fig. 8(a) and (b). Fig. 8(c) and (d) shows the magnetic

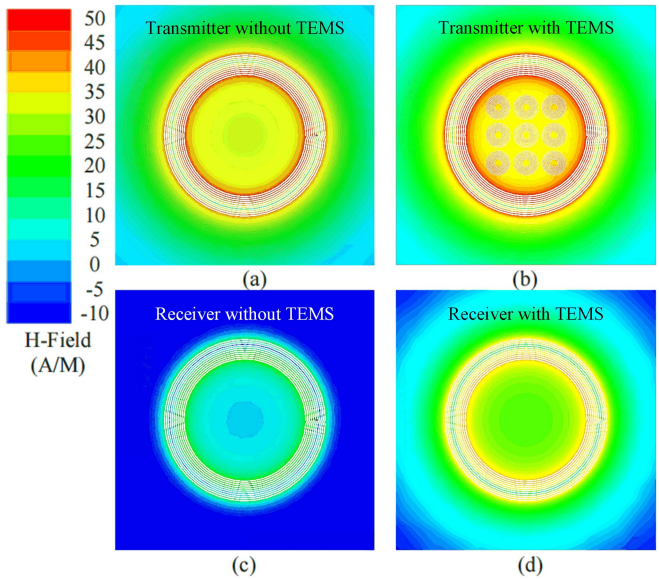

Fig. 8. Magnetic field strength distribution around transmitters and receiver. (a) Transmitter without TEMS. (b) Transmitter with TEMS. (c) Receiver without TEMS. (d) Receiver with TEMS.

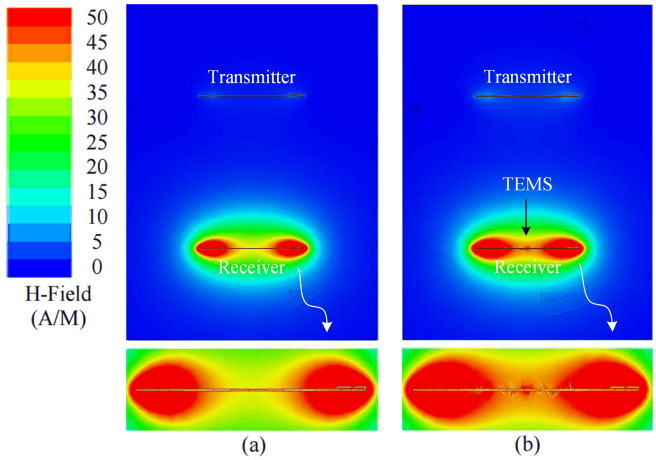

Fig. 9. Magnetic field strength distribution of the WPT system. (a) System without TEMS. (b) System with the proposed TEMS.

intensity around receivers of the WPT systems with and without the TEMS. Compared to the WPT system without TEMS, the magnetic intensity around the receiver of the TEMS-based WPT system is effectively improved. Considering the input power and load is constant, the enhanced magnetic field strength around the receiver coil corresponds to the increased current, accordingly, the output power of the load is increased. Besides, to confirm the effect of the TEMS, the magnetic field strength distribution in the transmission path of systems is shown in Fig. 9. As shown in Fig. 9, the magnetic field around the receiver coil will be increased with the proposed TEMS, and the magnetic field in around the TEMS is effectively modified.

Considering the simulation is conducted under the constant input power condition, it is difficult to maintain identical input

currents for the two aforementioned systems. Hence, the verification of leakage flux reduction is given in the following section with open-circuit experiments.

IV. Experimental Verification

The prototype of the proposed design is implemented and three separate experiments are conducted. The first open-circuit experiment is conducted to verify that the proposed TEMS can reduce the leakage flux and increase the coupling coefficient of the WPT system. The second and third experiments are conducted to verify the enhancement of efficiency caused by TEMS based on the scattering parameter [24], [25], [26], [27] and circuit model [30]. To distinguish those two efficiencies, the efficiency based on the scattering parameter is defined as transmission gain. The corresponding verification systems for the three experiments are different. The first system consists signal generator (TG5011) and oscilloscope and the second for transmission gain is with the spectrum analyzer and vector network analyzer (VNA) and SVA-1032X. The third system for efficiency measurement consisted of the signal generator (TG5011) and the power amplifier (A075). The cost associated with TEMS manufacturing includes expenses for copper wire, compensation capacitors, and 3-D printing FR4 slab. The proposed TEMS increase the cost by 13.5% of the transmitter coil with FR4 slab.

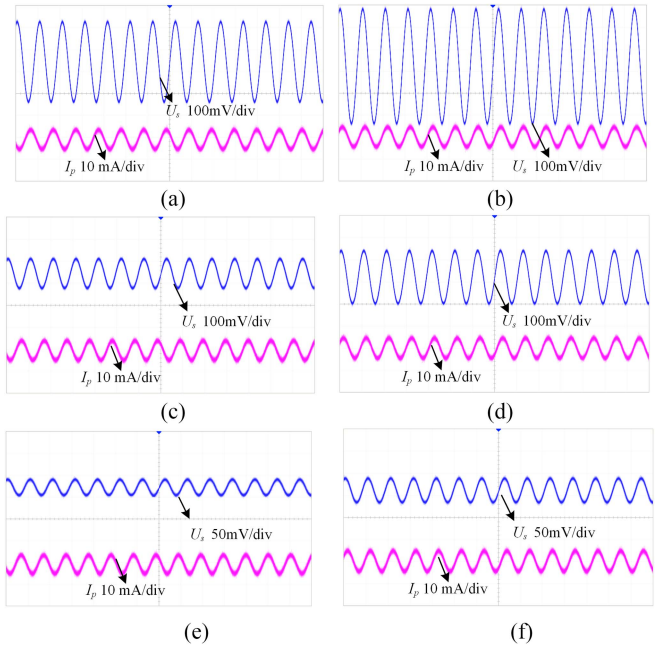

Fig. 10. Induced voltage U_s versus primary current i of the WPT systems. (a) Without TEMS under 100 mm. (b) With TEMS under 100 mm. (c) Without TEMS under 150 mm. (d) With TEMS under 150 mm. (e) With TEMS under 150 mm. (c) Without TEMS under 250 mm. (f) With TEMS under 250 mm.

A. Leakage Flux and Coupling Coefficient Verification

As for a coil, the flux ϕ in the magnetic circuit is related to the magnetomotive force F and the magnetic reluctance R_m, defined as follows:

$$\phi = \frac{F}{R_m} = \frac{Ni}{R_m} \tag{15}$$

where N and i is the number of turns of the coil and the current through the coil.

In the two-coil WPT system, the flux ϕ consisted of the main flux ϕ_m and the leakage flux ϕ_l, given as

$$\phi = \phi_m + \phi_l. \tag{16}$$

The main flux ϕ_m through the receiver coil and generate the induced voltage U_s, which follows:

$$U_s = N\frac{d\phi_m}{dt}. \tag{17}$$

Based on (15), with the same excitation current i, number of turns of the source coil and transfer distance, the flux ϕ for the WPT system with and without the proposed TEMS is the same. Accordingly, based on (16) and (17), with the same operating frequency, the induced voltage U_s of the receiver coil is proportional to the main flux ϕ_m, correspondingly observing the leakage flux ϕ_l. The induced voltage U_s versus primary current i of the WPT system with and without the proposed TEMS under different transfer distances is given in Fig. 10.

As indicated in Fig. 10, under transfer distances of 100, 150, and 250 mm, the proposed TEMS can effectively increase the induced voltage in the receiver coil from 67.18, 25.1, and 8.31 mV to 90.54, 42.43, and 11.14 mV. The increase in induced voltage U_s with the same excitation current i corresponding to the increased main flux ϕ_m and reduced leakage flux ϕ_l under a constant flux ϕ. Hence, the proposed TEMS can effectively reduce the leakage flux.

Apart from the reduced leakage flux, the proposed TEMS can also increase the mutual inductance, accordingly, the coupling coefficient of the WPT system. The verification process is given as follows.

As for the two-coil WPT system, the induced voltage U_s in the receiver coil is determined by the mutual inductance and current in the transmitter coil i_p, defined as follows:

$$U_s = j\omega M i_p \tag{18}$$

where ω and M are the circular frequency and mutual inductance of the WPT system, respectively.

Based on (18) and Fig. 10, the mutual inductance and coupling coefficient can be obtained, which is given in Fig. 11. As given in Fig. 11, the proposed TEMS can effectively increase the coupling coefficient of the WPT system. This is the fundamental issue of efficiency enhancement caused by the proposed TEMS.

B. Transmission Gain Verification

As for all the two-port systems, transmission gain G_t can be used to evaluate coil-to-coil efficiency based on scattering parameters. The VNA is an ideal solution to evaluate the G_t under the fully load-matching condition, which has been widely used in metasurface-based WPT systems [24], [25], [26]. As described in the previously proposed solutions, the entire WPT system with and without the metamaterial can be regarded as a two-port network consisting of the transmitter and receiver.

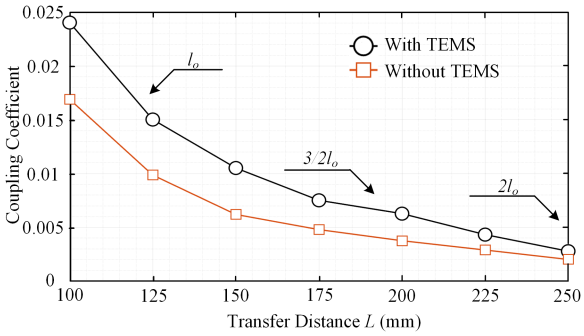

Fig. 11. Coupling coefficient of the WPT system with and without the proposed TEMS.

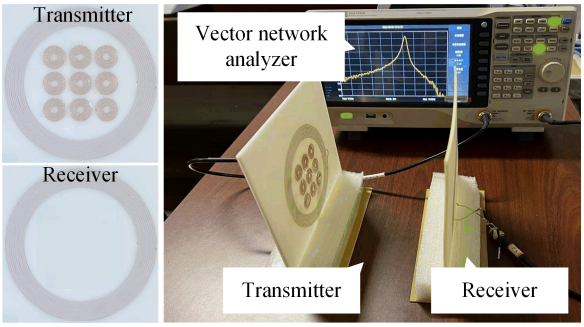

Fig. 12. Verification system of the WPT system with the TEMS.

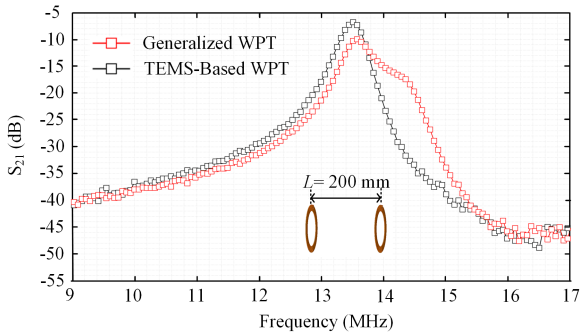

Fig. 13. Transmission gain versus frequency of the WPT systems with and without the proposed TEMS under the distance of 200 mm.

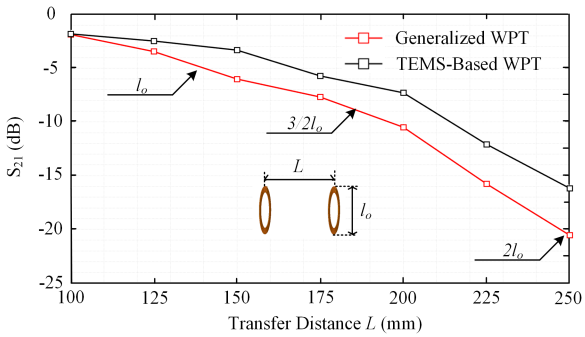

Fig. 14. Transmission gain versus transfer distance of the WPT system with and without the proposed TEMS.

By measuring the forward transmission coefficient S_{21}, the transmission gain/ coil-to-coil efficiency based on the scattering parameter is obtained.

The verification system of the transmission gain is shown in Fig. 12. The transmitter and receiver are connected to ports 1 and 2 of the VNA.

The relationship between coefficients, i.e., S_{11}, S_{21}, and transmission gain G_t is reported in [24] and [25], which is given as follows:

$$G_t = \frac{\left(1-|\Gamma_s|^2\right)\left(1-|\Gamma_s|^2\right)S_{21}^2}{|((1-S_{11}\Gamma_s)(1-s_{22}\Gamma_L)-S_{12}S_{21}\Gamma_s\Gamma_L)|}) \quad (19)$$

where Γ_L and Γ_S represent the reflection coefficient at the source (transmitter) and load (receiver), defined as

$$\Gamma_S = \frac{Z_S - Z_0}{Z_S + Z_0} \quad (20)$$

$$\Gamma_L = \frac{Z_L - Z_0}{Z_L + Z_0} \quad (21)$$

where Z_S, Z_L, and Z_0 are the source impedance, load impedance, and reference impedance, respectively.

Besides, the overall efficiency of the system is defined as

$$\eta_{\text{system}} = G_t * \eta_{\text{converter}} \quad (22)$$

where G_t and $\eta_{\text{converter}}$ is the efficiency determined by the coil and the applied converter.

In the VNA verification system, The impedances of the source and the load are matched to the reference impedance 50 Ω, ($Z_S = Z_0$). The converter is removed from the verification system. Hence, the impact of converter and load-matching issues on efficiency is eliminated, making Γ_S and Γ_L both zero.

Hence, by substituting (19)–(21) into (22), the efficiency based on the scattering parameter is expressed as follows:

$$\eta_{\text{system}} = G_t = S_{21}^2. \quad (23)$$

Yin et al. [30] proposed another definition of transmission gain given as (24), which takes the reflection coefficient into account

$$G_t = \frac{S_{21}^2}{1-S_{11}^2}. \quad (24)$$

However, based on the results in [31], the G_t calculated based on (23) is closer to the measured efficiency compared to that based on (24). Hence, in most of the metasurface-based WPT systems [24], [25], [26], [27], (23) is used to evaluate the transmission gain.

The transmission gain S_{21} of the WPT systems with and without the proposed TEMS under the rated transfer distance of 200 mm is shown in Fig. 13 while the S_{21} versus transmission distance is given in Fig. 14.

As shown in Fig. 13, under the rated transfer distance of 200 mm, the WPT system without TEMS reaches the peak transmission gain of −10.49 dB while the proposed TEMS achieves a transmission gain improvement of 30.5%, reaching −7.29 dB.

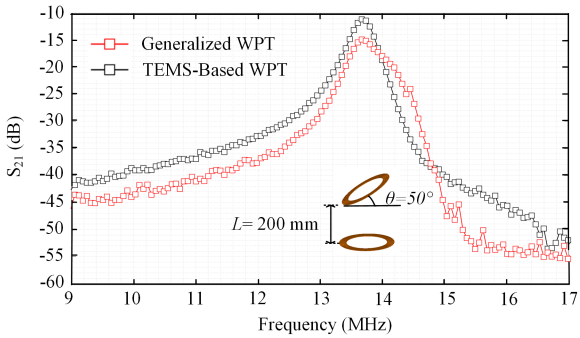

Fig. 15. Transmission gain versus frequency of the WPT systems with and without the proposed TEM under angular misalignment θ of 50°.

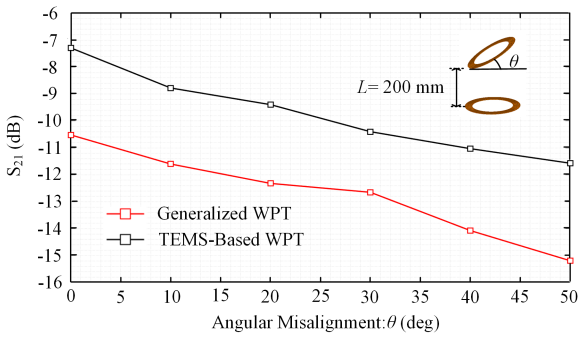

Fig. 16. Transmission gain versus angular misalignment of the WPT system with and without the proposed TEMS under the transfer distance of 200 mm.

As shown in Fig. 14, the transmission gain improvement of the WPT system with TEMS will rise with the increase of the transfer distance.

In practical applications, the TEMS is installed in the transmitter and placed in the charging platform together with the transmitter under a fixed position. Hence, the angular and parallel misalignment conditions are inevitable, which are investigated as follows.

The transmission gain S_{21} versus frequency of the WPT systems with angular misalignment of 50° and the distance of 200 mm is given in Fig. 15. The angular misalignment θ variation versus S_{21} is indicated in Fig. 16. As shown in Fig. 15, under the abovementioned condition, the WPT system with TEMS reaches the peak transmission gain of −11.57 dB while the conventional WPT system only reaches −15.19 dB.

The transmission gain S_{21} versus frequency of the WPT systems with parallel misalignment of 70 mm and the distance of 200 mm is given in Fig. 17. The parallel misalignment d variation versus S_{21} is indicated in Fig. 18.

As shown in Fig. 17, the TEMS can effectively increase the S_{21} of the WPT system from −16.65 dB to −13.51 dB. Besides, the S_{21} enhancement will increase with the increase of the misalignment level. Transmission gain versus parallel misalignment distance under the transfer distance of 200 mm is given in Fig. 18.

Fig. 17. Transmission gain versus frequency of the WPT systems with and without the proposed TEMS under parallel misalignment d of 70 mm and transfer distance of 200 mm.

Fig. 18. Transmission gain versus parallel misalignment distance of the WPT systems with and without the TEMS under the distance of 200 mm.

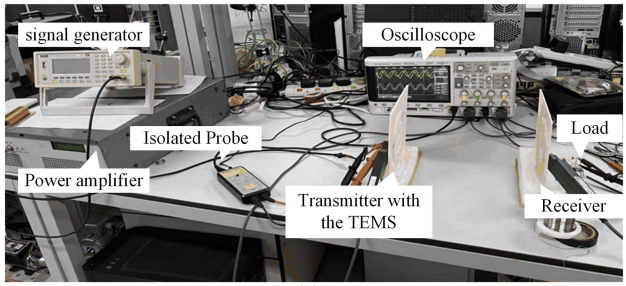

(a)

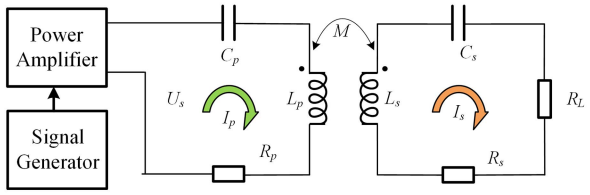

(b)

Fig. 19. Efficiency verification system of the TEMS based WPT system. (a) Verification system. (b) Schematic diagram of the verification system.

C. Power Transfer Efficiency Verification

As for the coil-to-coil efficiency based on the circuit model, the verification system consisting of the signal generator and power amplifier and the corresponding circuit diagram, are given

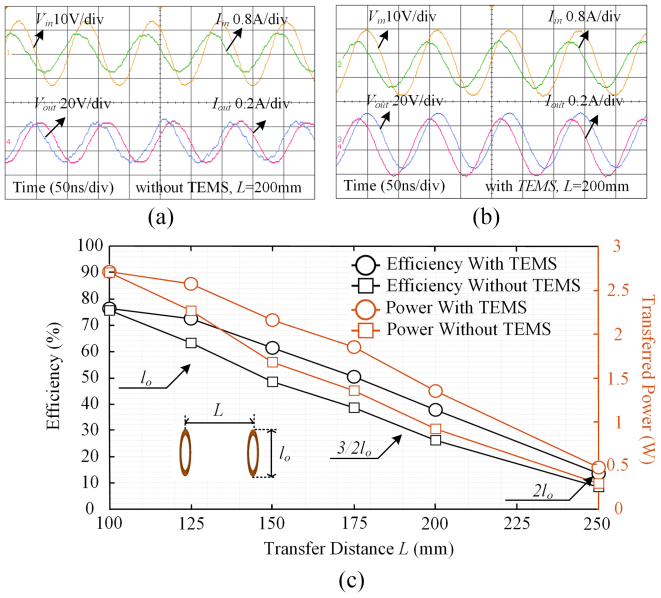

Fig. 20. Experimental results of the WPT system with/without the proposed TEMS. (a) WPT system without TEMS with $L = 200$ mm. (b) WPT system with TEMS with $L = 200$ mm. (c) Efficiency versus transfer distance.

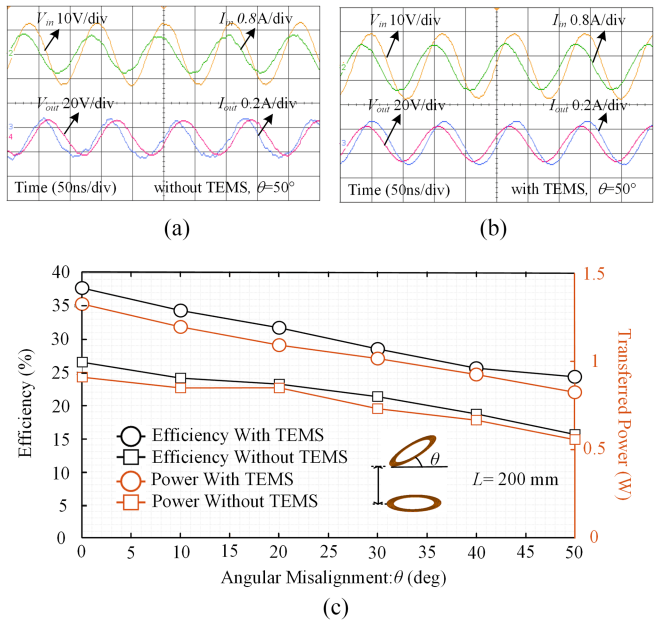

Fig. 21. Experimental results of the WPT system with/without the proposed TEMS with angular misalignment. (a) WPT system without TEMS with $\theta = 50°$. (b) WPT system with TEMS with t $\theta = 50°$. (c) Efficiency versus angular misalignment θ variation.

in Fig. 19. The load is 40 Ω and the compensation network is selected as series–series topology.

The coil-to-coil efficiency of the system based on the circuit model [30] is defined as follows:

$$\eta_{\text{system}} = \frac{P_{\text{out}}}{P_{\text{in}}} = \frac{U_{\text{in}} I_{\text{in}} \cos\theta_{\text{in}}}{U_{\text{out}} I_{\text{out}} \cos\theta_{\text{out}}} \tag{25}$$

where the U_{in}, I_{in}, U_{out}, I_{out}, θ_{in}, and θ_{out} are the input and output voltage, current, and corresponding angle differences, respectively. P_{out} and P_{in} is the output and input power.

The experimental results of the WPT system with and without the proposed TMES under transfer distances of 200 mm are shown in Fig. 20(a) and (b). The WPT system with the proposed TEMS reaches efficiencies of 37.7% while that without the TEMS only reaches 26.1%. With the constant input power, the output power will decrease with the increase of transfer distance. Correspondingly, the coil-to-coil efficiency indicates the same trend.

The coil-to-coil efficiency and output power versus transfer distance L of the WPT system with and without TEMS are given in Fig. 20(c). As shown in Fig. 20(c), the coil-to-coil efficiency variation indicates the same trend with transmission gain given in Fig. 14. Under the transfer distance of 100 mm, the efficiency between the proposed TEMS-based WPT system and the conventional solution is minimal, indicating that the effective operating distance of the TEMS is more than 100 mm.

D. Misalignments Analysis

The receiver is installed in the electromagnetic device, hence, parallel misalignment and angular misalignment cannot be avoided. The proposed TEMS eliminates the misalignment issue with the transmitter coil, indicating a key advantage compared to the generalized metasurface-based WPT system.

The efficiency of the system with and without TEMS with receiver angular misalignment of 50° is shown in Fig. 21(a) and (b). As shown in Fig. 21(a) and (b), the efficiency of the system with and without the TEMS is 24.3% and 15.6%, respectively. The performance of the systems with angular misalignment from 0 to 50° is shown in Fig. 21(c). As shown in Fig. 21(c), despite the efficiency of the WPT systems with and without the proposed TEMS will both decrease with the increase of the angular misalignment degree, the TEMS can always increase the efficiency of the system.

Fig. 22(a) and (b) indicates the experimental waveforms of the WPT system with and without the proposed TEMS under parallel misalignment of 70 mm. The efficiency of the system with and without the TEMS under the parallel misalignment of 70 mm is 19.6% and 13.5%. Fig. 22(c) demonstrates the performance of the systems under different parallel misalignments d. The efficiency of the system without and with TEMS will decrease with the increase of the parallel misalignments d. However, the proposed TEMS can maintain a stable improvement of the efficiency under the parallel misalignment within 70 mm, which is no less than 34.8%.

A comprehensive comparison between the proposed TEMS and generalized solutions is shown in Table III. Compared to the solutions given in Table III, the key merits of the proposed TEMS among generalized solutions are the efficiency improvement per volume and no additional space occupation. Along with reducing the relative dimensions by 24.2% to 160.5%, the proposed structure still can increase efficiency effectively compared to the previously proposed solutions given in Table III.

TABLE III
COMPREHENSIVE COMPARISON OF THE PREVIOUSLY REPORTED METAMATERIAL-BASED SYSTEMS AND THE PROPOSED TEMS

Categorization	Operating Frequency (MHz)	Diameter of Tx/Rx Coils (mm)	Diameter of MTM/MTS Slabs (mm)	Property of MTM/ MTS	Diameter Ratio of MTM/ MTS Slab and Rx/Tx (%)	Rated Transfer Distance (mm)	Efficiency/ improvement with MTM (%)
This paper: TEMS	13.56	124	94	Negative	75.8	200	37.7/42.2
[17]: MTM in the middle	58	92	150	Negative	163.1	200	13.5/75.5
[22]: MTM in the middle	6.78	150	260.4	Negative	173.3	200	10.7/73.8
[24]: Dual-band MTM slab	13.56/27.12	165/93	390	0/Negative	236.3	250	26.9/102.6
[29]: Cubic MTM in the middle	560	30	30	0	100	100	10.2/66.6
[26]: Dual MTM in back side	13.56	200	360	0	180	300	36.2/33.7
[32]: Single MTM in the middle	26.65	45/36	69	-1	153.3	79	18.2/37.9

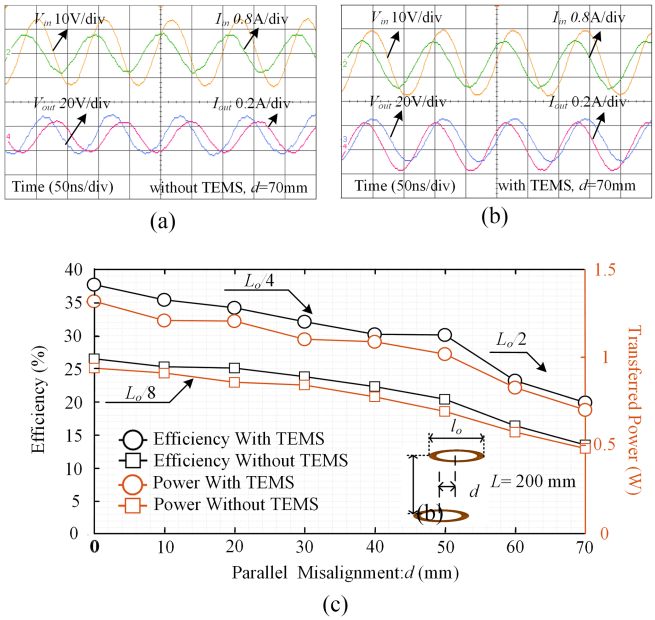

Fig. 22. Experimental results of the WPT system with/without the proposed TEMS with angular misalignment. (a) WPT system without TEMS with $d = 70$ mm. (b) WPT system with TEMS with $d = 70$ mm. (c) Efficiency versus parallel misalignment.

V. CONCLUSION

This article proposes and implements a transmitter-embedded metasurface for the 13.56 MHz wireless power transfer system with an extended transfer distance. The mathematical model of the metamaterial and the theoretical feasibility of the overall system are established. The contributions of this article are summarized as follows.

1) A highly practical metamaterial-based WPT system is achieved, with increased efficiency obtained without occupying additional space excluding the occupation of the transmitter coil. Incorporated into the designed topology, the power transfer efficiency and transmission gain are enhanced by 14.5% to 62.7% across various transfer distances.
2) The proposed TEMS is validated under angular and parallel misalignment conditions. It exhibits efficiency enhancement under angular misalignment of 50° (no less than 33.8%) and parallel misalignment of 70 mm (not less than 34.8%).
3) A higher transfer efficiency promotion with reduced volume is achieved. Along with reducing the relative dimensions by 24.2% to 160.5%, the proposed TEMS still can increase efficiency/transmission gain effectively.
4) The flux is focused on the receiver coil, the leakage flux is reduced, and the mutual inductance between coils is increased with the proposed TEMS.

Effective efficiency promotion, no additional space occupation, and leakage flux reduction are simultaneously presented in the proposed design, which confirms its superiority in extended-distance WPT systems.

REFERENCES

[1] P. Zhang et al., "Wireless power transfer-based voltage equalizer for scalable cell-string charging," *IEEE Trans. Ind. Electron.*, vol. 71, no. 1, pp. 493–503, Jan. 2024.
[2] Y. Yang, W. Zhong, S. Kiratipongvoot, S.-C. Tan, and S. Y. R. Hui, "Dynamic improvement of series–series compensated wireless power transfer systems using discrete sliding mode control," *IEEE Trans. Power Electron.*, vol. 33, no. 7, pp. 6351–6360, Jul. 2018.
[3] P. Zhang, M. Saeedifard, O. C. Onar, Q. Yang, and C. Cai, "A field enhancement integration design featuring misalignment tolerance for wireless EV charging using LCL topology," *IEEE Trans. Power Electron.*, vol. 36, no. 4, pp. 3852–3867, Apr. 2021.
[4] Y. Yang, "Precise modeling of nonlinear rectifier loads in wireless power transfer systems," *IEEE Trans. Emerg. Sel. Topics Power Electron.*, vol. 11, no. 3, pp. 3574–3585, Jun. 2023.
[5] Y. Zhang, T. Lu, Z. Zhao, F. He, K. Chen, and L. Yuan, "Employing load coils for multiple loads of resonant wireless power transfer," *IEEE Trans. Power Electron.*, vol. 30, no. 11, pp. 6174–6181, Nov. 2015.
[6] H. Lin, S. Niu, Z. Xue, and S. Wang, "A simplified virtual-vector-based model predictive control technique with a control factor for three-phase SPMSM drives," *IEEE Trans. Power Electron.*, vol. 38, no. 6, pp. 7546–7557, Jun. 2023,.
[7] H. Lin et al., "Three-stage duty cycle-based deadbeat predictive torque control for three-phase SPMSMs with CMV reduction," *IEEE Trans. Power Electron.*, vol. 38, no. 9, pp. 11385–11398, Sep. 2023, doi: 10.1109/TPEL.2023.3288184.
[8] X. Zhang, S. L. Ho, and W. N. Fu, "A hybrid optimal design strategy of wireless magnetic-resonant charger for deep brain stimulation devices," *IEEE Trans. Magn.*, vol. 49, no. 5, pp. 2145–2148, May 2013.
[9] X. Zhang, X. Zhang, and L. Han, "An energy efficient internet of things network using restart artificial bee colony and wireless power transfer," *IEEE Access*, vol. 7, pp. 12686–12695, 2019.
[10] C. Cheng, Z. Zhou, W. Li, C. Zhu, Z. Deng, and C. C. Mi, "A multi-load wireless power transfer system with series-parallel-series compensation," *IEEE Trans. Power Electron.*, vol. 34, no. 8, pp. 7126–7130, Aug. 2019.
[11] J. Shin et al., "Design and implementation of shaped magnetic-resonance-based wireless power transfer system for roadway-powered moving electric vehicles," *IEEE Trans. Ind. Electron.*, vol. 61, no. 3, pp. 1179–1192, Mar. 2014.
[12] C. Cai, J. Wang, F. Zhang, X. Liu, P. Zhang, and Y.-G. Zhou, "A multichannel wireless UAV charging system with compact receivers for improving transmission stability and capacity," *IEEE Syst. J.*, vol. 16, no. 1, pp. 997–1008, Mar. 2022.
[13] C. Cheng et al., "A multiload inductive power transfer repeater system with constant load current characteristics," *IEEE J. Emerg. Sel. Topics Power Electron.*, vol. 8, no. 4, pp. 3533–3541, Dec. 2020.

[14] C. Cai, M. Saeedifard, J. Wang, P. Zhang, J. Zhao, and Y. Hong, "A cost-effective segmented dynamic wireless charging system with stable efficiency and output power," *IEEE. Trans. Power Electron.*, vol. 37, no. 7, pp. 8682–8700, Jul. 2022.
[15] W. Zhang, S. C. Wong, C. K. Tse, and Q. Chen, "Design for efficiency optimization and voltage controllability of series–Series compensated inductive power transfer systems," *IEEE Trans. Power Electron.*, vol. 29, no. 1, pp. 191–200, Jan. 2014.
[16] X. Liu and G. Wang, "A novel wireless power transfer system with double intermediate resonant coils," *IEEE Trans. Ind. Electron.*, vol. 63, no. 4, pp. 2174–2180, Apr. 2016.
[17] J. Li, J.-K. Lin, X. Song, S. Yan, K.-D. Xu, and X. Y. Zhang, "Efficiency-enhanced wireless power transfer based on multiple coupling paths," *IEEE Microw. Wireless Compon. Lett.*, vol. 32, no. 5, pp. 444–447, May 2022.
[18] N. Oshimoto, K. Sakuma, and N. Sekiya, "Improvement in power transmission efficiency of wireless power transfer system using superconducting intermediate coil," *IEEE Trans. Appl. Supercond.*, vol. 33, no. 5, Aug. 2023, Art. no. 1501004, doi: 10.1109/TASC.2023.3256342.
[19] J. Besnoff, M. Chabalko, and D. S. Ricketts, "A frequency-selective zero-permeability metamaterial shield for reduction of near-field electromagnetic energy," *IEEE Antennas Wireless Propag. Lett.*, vol. 15, pp. 654–657, 2016.
[20] X. Zhang, S. L. Ho, and W. N. Fu, "Quantitative analysis of a wireless power transfer cell with planar spiral structures," *IEEE Trans. Magn.*, vol. 47, no. 10, pp. 3200–3203, Oct. 2011.
[21] W. Yang, S.-L. Ho, and W. Fu, "Numerical and experimental study on design optimization of hybrid metamaterial slab for wireless power transmission," *IEEE Access*, vol. 8, pp. 82700–82708, 2020.
[22] Y. Cho et al., "Thin hybrid metamaterial slab with negative and zero permeability for high efficiency and low electromagnetic field in wireless power transfer systems," *IEEE Trans. Electromagn. Compat.*, vol. 60, no. 4, pp. 1001–1009, Aug. 2018.
[23] T. Shaw and D. Mitra, "Wireless power transfer system based on magnetic dipole coupling with high permittivity metamaterials," *IEEE Antennas Wireless Propag. Lett.*, vol. 18, no. 9, pp. 1823–1827, Sep. 2019.
[24] C. Lu, X. Huang, C. Rong, X. Tao, Y. Zeng, and M. Liu, "A dual-band negative permeability and near-zero permeability metamaterials for wireless power transfer system," *IEEE Trans. Ind. Electron.*, vol. 68, no. 8, pp. 7072–7082, Aug. 2021.
[25] C. Lu, X. Huang, X. Tao, C. Rong, and M. Liu, "Comprehensive analysis of side-placed metamaterials in wireless power transfer system," *IEEE Access*, vol. 8, pp. 152900–152908, 2020.
[26] C. Lu et al., "Investigation of negative and near-zero permeability metamaterials for increased efficiency and reduced electromagnetic field leakage in a wireless power transfer system," *IEEE Trans. Electromagn. Compat.*, vol. 61, no. 5, pp. 1438–1446, Oct. 2019.
[27] J. Zhou, P. Zhang, J. Han, L. Li, and Y. Huang, "Metamaterials and metasurfaces for wireless power transfer and energy harvesting," *Proc. IEEE*, vol. 110, no. 1, pp. 31–55, Jan. 2022.
[28] Z. Gong and S. Yang, "One-dimensional stacking miniaturized low-frequency metamaterial bulk for near-field applications," *J. Appl. Phys.*, vol. 127, no. 11, 2020, Art. no. 114901.
[29] R. Das, A. Basir, and H. Yoo, "A metamaterial-coupled wireless power transfer system based on cubic high-dielectric resonators," *IEEE Trans. Ind. Electron.*, vol. 66, no. 9, pp. 7397–7406, Sep. 2019.
[30] Y. Yin, H. Li, and M. Fu, "Inductive coupler analysis based on scattering parameters with nonstandard terminal impedance," *IEEE J. Emerg. Sel. Topics Ind. Electron.*, vol. 3, no. 4, pp. 1168–1176, Oct. 2022.
[31] M. Song, P. Belov, and P. Kapitanova, "Wireless power transfer based on dielectric resonators with colossal permittivity," *Appl. Phys. Lett.*, vol. 109, Dec. 2016, Art. no. 223902.
[32] A. Rajagopalan, A. K. RamRakhyani, D. Schurig, and G. Lazzi, "Improving power transfer efficiency of a short-range telemetry system using compact metamaterials," *IEEE Trans. Microw. Theory Techn.*, vol. 62, no. 4, pp. 947–955, Apr. 2014.

Yuanxi Chen (Student Member, IEEE) received the B.Eng. degree in electronic science and technology and M.Eng. degree in electrical engineering from Huaqiao University, Xiamen, China, in 2015 and 2018, respectively, and the Ph.D. degree in electrical and electronic engineering from The Hong Kong Polytechnic University, Hong Kong, in 2023.

His research interests include electric machines, electromagnetic metamaterial, transformer, and wireless power transmission.

Xing Zhao (Member, IEEE) received the B.Eng. degree from Nanjing University of Aeronautics and Astronautics, Nanjing, China, in 2014, and the Ph.D. degree from The Hong Kong Polytechnic University, Hong Kong, in 2020, both in electrical engineering.

From 2019 to 2020, he was a Visiting Research Scholar with the Center for Advanced Power Systems, Florida State University, Tallahassee, USA. Between 2020 and 2021, he was a Research Assistant Professor with the Department of Electrical Engineering, The Hong Kong Polytechnic University. Since 2021, he has been a Lecturer with the Department of Electronic Engineering, University of York, U.K. He has authored or coauthored more than 50 technical papers in the international journals and conferences and holds six granted patents. His research interests include advanced electrical machines, motor drives, and power electronics for electric vehicles and renewable energy systems.

Shuangxia Niu (Senior Member, IEEE) received the B.Sc. and M.Sc. degrees from Tianjin University, Tianjin, China, in 2002 and 2005, respectively, and the Ph.D. degree from the University of Hong Kong, Hong Kong, in 2009, all in electrical engineering.

Since 2009, she has been with The Hong Kong Polytechnic University, Hong Kong. She is currently a Professor with the Department of Electrical and Electronic Engineering, Hong Kong Polytechnic University, Hong Kong. She has authored more than 100 papers in leading journals. She was an Associate Editor for the IEEE JOURNAL OF EMERGING AND SELECTED TOPICS IN POWER ELECTRONICS. Her research interests include electrical machines and drives for electric vehicles, renewable energy, and applied electromagnetics.

Weinong Fu received the Ph.D. degree in electrical engineering from The Hong Kong Polytechnic University (PolyU), Hong Kong, in 1999.

He is a Professor with Shenzhen Institutes of Advanced Technology, Chinese Academy of Sciences. He was with PolyU about 13 years as an Associate Professor and Full Professor. He was one of the key developers at Ansoft Corporation in Pittsburgh, USA. He has about seven years of working experience at Ansoft, focusing on the development of commercial software Maxwell. He has made many contributions to the theory and application of electromagnetic field computation and electric device design, including the publication of more than 250 refereed journal papers. His research interests include computational electromagnetics, optimal design of electric devices, applied electromagnetics, and novel electric machines.

Hongjian Lin (Senior Member, IEEE) received the Ph.D. degree in electrical engineering from Southwest Jiaotong University, Chengdu, China, in 2021.

From 2019 to 2020, he was a Visiting Researcher with the School of Electrical and Computer Engineering, Georgia Institute of Technology, Atlanta, GA, USA. He was a Postdoc Research Associate with The Hong Kong Polytechnic University, Hong Kong. He is currently a Postdoc Research Associate with the Department of Electrical Engineering, City University of Hong Kong. His research interests include predictive model control of converters in microgrids, electrical machines and drives control, wireless power transfer control, electric traction supply system, magnetic field analysis, and modulation and control technologies of multilevel converters in the solid-state transformer.